Ground effects on the stability of separated flow around a NACA 4415 airfoil at low Reynolds numbers

Wei He[a,*], Peng Yu[b], Larry K. B. Li[a]

[a] *The Hong Kong University of Science and Technology, Clear Water Bay, Hong Kong*
[b] *Southern University of Science and Technology, Shenzhen, China*

Abstract

We perform a linear BiGlobal modal stability analysis on the separated flow around a NACA 4415 airfoil at low Reynolds numbers ($Re = 300$–1000) and a high angle of attack ($\alpha = 20°$), with a focus on the effect of the airfoil's proximity to two different types of ground: a stationary ground and a moving ground. The results show that the most dominant perturbation is a Kelvin–Helmholtz mode, which gives rise to a supercritical Hopf bifurcation to a global mode, leading to large-scale vortex shedding at a periodic limit cycle. As the airfoil approaches the ground, this mode can become more unstable or less unstable, depending on the specific type of ground: introducing a stationary ground to an otherwise groundless system is destabilizing but introducing a moving ground is stabilizing, although both effects weaken with increasing Re. By performing a Floquet analysis, we find that short-wavelength secondary instabilities are damped by a moving ground but are amplified by a stationary ground. By contrast, long-wavelength secondary instabilities are relatively insensitive to ground type. This numerical–theoretical study shows that the ground can have an elaborate influence on the primary and secondary instabilities of the separated flow around an airfoil at low Re. These findings could be useful for the design of micro aerial vehicles and for improving our understanding of natural flyers such as insects and birds.

Keywords: ground effect, separation, flow instability, modal analysis

1. Introduction

When an aircraft lands on or takes off from a runway, it flies slowly but at a high angle of attack, potentially causing the flow over its wings and control surfaces (e.g. flaps and slats) to separate. However, the aircraft can still be more aerodynamically efficient than in free flight as a result of its close proximity to the ground, a phenomenon known as the ground effect [1]. This effect has been exploited not just in conventional aircraft but also in vehicles specifically designed to fly close to the ground (e.g. A-90 Ekranoplan). The aerodynamic performance of such Wing-In-Ground-effect (WIG) vehicles has been reviewed by Halloran

*Corresponding author
Email address: mewhe@ust.hk (Wei He)

and O'Meara [2] and Rozhdestvensky [3]. Besides playing a role in large-scale aircraft [4] and WIG vehicles [5], the ground effect can also influence the aerodynamic performance of micro aerial vehicles [6, 7] and natural flyers such as insects and birds [8, 9, 10].

Although the ground effect has already been extensively studied, previous efforts have focused mostly on moderate-to-high Reynolds numbers (Re) and low angles of attack (α), where large-scale flow separation is absent. As will be discussed below, a key aim of the present study is to investigate the ground effect at low Re and high α, where large-scale flow separation dominates the aft wake region.

1.1. Previous studies: numerical simulations and laboratory experiments

As mentioned above, most studies on the ground effect have been done at moderate-to-high Re and low α. For example, using a wind tunnel equipped with a moving ground, Ahmed et al. [11] conducted experiments on the flow around a NACA 4412 airfoil at $Re = 3 \times 10^5$. They found that, for $\alpha > 4°$, reducing the ground clearance led to an increase in the lift coefficient, which was caused by an increase in the pressure under the airfoil. Yang et al. [12] performed numerical simulations to investigate the aerodynamic performance of a WIG vehicle flying at 0.3 chord lengths above a curved surface at $Re = 6 \times 10^7$ and $\alpha = 0$–$5°$. They found that the pressure under the wing varies periodically in time, creating similarly periodic variations in the aerodynamic forces acting on the overall vehicle.

Using an immersed boundary–lattice Boltzmann method, Gao et al. [13] numerically simulated the flow around an insect model equipped with a 25%-thickness elliptical wing flapping near a wall at $Re = 100$. They found that the ground effect was particularly strong when the wing was within two chord lengths of the wall ($h < 2$) but weakened rapidly away from the wall, becoming negligible beyond six chord lengths ($h > 6$). Zhang et al. [14] examined the hydrodynamics of a flexible plate flapping close to a wall by applying a sinusoidal force to the leading edge of the plate. In numerical simulations, Li et al. [15] investigated the laminar flow past an inclined plate near the ground at $Re = 300$–1000 and $\alpha = 20$–$30°$, with a focus on the changes in wall shear stress along the ground.

Yang et al. [16] numerically studied the viscous flow around a NACA 0012 airfoil at $h = 0.1$, while Lu et al. [10] found that the force coefficients and vorticity distribution of a flapping wing in ground effect were qualitatively little changed over a wide range of Reynolds numbers: $Re = 100$–5000. Taira and Colonius [17] examined the three-dimensional low-Re flow past an inclined low-aspect-ratio flat plate and found that the flow topology did not vary significantly between low-Re numerical simulations and high-Re experiments [18].

Over the years, various efforts have been made to enhance the aerodynamic efficiency of WIG vehicles [3]. One notable example is the development of the power-augmented ram (PAR) configuration, which involves mounting the engines forward of the wing, enabling them to blow high-speed exhaust gases under the wing, enhancing the air cushion there and thus increasing lift, which is particularly useful for take-off. Yang and Yang [19] assessed the ability of PAR in increasing the lift of a WIG vehicle and found that, when the wings were lowered from $h = 0.3$ to 0.1, lift increased while drag decreased, which is consistent with the trends observed in most WIG vehicles [3]. Recently, Qin et al. [20] numerically investigated the aerodynamic forces acting on a wing–canard configuration in ground effect at $\alpha = 12°$.

They found that reducing the ground clearance led to an increase in lift owing to changes in the windward-surface pressure distribution and the formation of leading-edge vortices.

1.2. Previous studies: linear local and global stability analyses

At low α, the stability of the flow around an airfoil in free flight (i.e. without ground effects) has been the subject of numerous studies. Theofilis and Sherwin [21] and Theofilis et al. [22] performed linear local and global stability analyses on the flow around a NACA 0012 airfoil at low α and found the dominant instability to be a Kelvin–Helmholtz (KH) mode. Loh et al. [23] examined the transient growth of a similar airfoil at high Re and low α. They found the optimal perturbation for energy growth to be controlled by two-dimensional mechanisms, with the Orr mechanism being the primary cause of vortex shedding.

At high α, large-scale flow separation occurs. Kitsios et al. [24] and Rodríguez and Theofilis [25] analyzed the stability of the separated flow behind an airfoil at low Re and found the dominant instability to be a stationary mode. For separated flow past a NACA 0015 airfoil at $Re = 500$, Gioria et al. [26] and He et al. [27] found the leading modal instability to be a KH mode, with the optimal initial perturbations, calculated via a non-modal analysis, evolving towards this mode. Using linear stability analysis, Zhang and Samtaney [28] investigated the separated flow past a NACA 0012 airfoil at $Re = 400$–1000 and found that the recirculation zone grows with Re, with two oscillatory modes appearing at a KH-dominated spanwise wavenumber of $\beta = 1$ when $Re = 800$–1000. Using Floquet analysis, Tsiloufas et al. [29] and Brehm and Fasel [30] examined secondary instabilities in the flow past NACA airfoils, while He et al. [27] used short-wavelength secondary modes to recover the stall cells seen in experiments on cylinder wakes [31, 32] and airfoils [33, 34].

An industrial flow configuration that resembles an airfoil in ground effect is that of compressor or turbine cascades. Analyzing the flow through a low-pressure compressor cascade, Abdessemed et al. [35] found the dominant instability to be a long-wavelength secondary mode. Sharma et al. [36] and Rocco et al. [37] used a non-modal stability analysis to study the flow through a set of low-pressure turbine blades and found that transient growth can excite a wake mode. He et al. [38] analyzed the linear stability of the wake behind an elliptical laminar wing and found that the most amplified instability can disrupt the flow structures connecting wing-tip vortices but has little effect on wing-tip vortex formation and development. Despite these various studies, however, relatively little has been done to date to systemically analyze the primary or secondary instability of the flow around an airfoil positioned at different heights above a stationary or moving ground, especially at the low-Re, high-α conditions expected in the separated flow around micro aerial vehicles [6, 7].

1.3. Contributions of the present study

In this numerical–theoretical study, we perform a linear BiGlobal modal stability analysis on the separated flow around a NACA 4415 airfoil at low Reynolds numbers ($Re = 300$–1000) and a high angle of attack ($\alpha = 20°$), with a focus on the effect of the airfoil's proximity to two different types of ground: (i) a stationary ground, which simulates an aircraft landing on a stationary runway, and (ii) a moving ground, which simulates an aircraft landing on a moving runway, e.g. an aircraft carrier. We also explore the interaction between the

separation bubble behind the airfoil and the boundary layer growing along the ground, as well as performing a Floquet analysis to examine secondary instabilities.

This paper is organized as follows. In Sec. 2, we present the theoretical framework underpinning linear BiGlobal modal stability analysis. In Sec. 3, we describe the numerical framework used to solve for the steady and unsteady base flows, including the mesh geometry and the boundary conditions. In Sec. 4, we discuss the results of the base-flow computations and the modal stability analysis, focusing on the effect of ground clearance and ground type on the growth rates and frequencies of the instability modes. In Sec. 5, we conclude by summarizing the key results and their implications for the design of micro aerial vehicles. A grid independence study is included in Appendix A.

2. Theoretical framework

The flow under consideration is governed by the incompressible Navier–Stokes and continuity equations:

$$\begin{aligned} \frac{\partial \mathbf{u}}{\partial t} + \mathbf{u}\cdot\nabla\mathbf{u} &= -\nabla p + \frac{1}{Re}\nabla^2\mathbf{u}, \\ \nabla\cdot\mathbf{u} &= 0, \end{aligned} \tag{1}$$

where the Reynolds number is defined as $Re \equiv U_\infty c/\nu$, with U_∞ as the free-stream velocity, c as the chord length of the airfoil, and ν as the kinematic viscosity of air. The dimensionless velocity vector and pressure are encapsulated in $\mathbf{q}(x,y,z,t) = (\mathbf{u},p)^{\mathrm{T}} = (u,v,w,p)^{\mathrm{T}}$.

Equation (1) is solved numerically to obtain a steady or time-periodic two-dimensional base flow $\bar{\mathbf{q}}(x,y,t) = (\bar{\mathbf{u}},\bar{p})^{\mathrm{T}}$, on which a linear BiGlobal modal stability analysis is performed [39, 40]. The stability analysis considers small-amplitude three-dimensional unsteady perturbations defined by $\tilde{\mathbf{q}}(x,y,z,t) = (\tilde{\mathbf{u}},\tilde{p})^{\mathrm{T}}$. Superimposing $\tilde{\mathbf{q}}$ onto $\bar{\mathbf{q}}$ leads to the reconstruction of the total field $\mathbf{q} = \bar{\mathbf{q}} + \epsilon\tilde{\mathbf{q}}$ where $\epsilon \ll 1$. Substituting this decomposition into Eqn. (1) yields the linearized Navier–Stokes equations:

$$\begin{aligned} \frac{\partial \tilde{\mathbf{u}}}{\partial t} + \bar{\mathbf{u}}\cdot\nabla\tilde{\mathbf{u}} + \tilde{\mathbf{u}}\cdot\nabla\bar{\mathbf{u}} &= -\nabla\tilde{p} + \frac{1}{Re}\nabla^2\tilde{\mathbf{u}}, \\ \nabla\cdot\tilde{\mathbf{u}} &= 0. \end{aligned} \tag{2}$$

In incompressible flow, the pressure disturbance is a function of the velocity disturbance, which implies that Eqn. (2) can be expressed as:

$$\frac{\partial \tilde{\mathbf{u}}}{\partial t} = \mathcal{L}\tilde{\mathbf{u}}, \tag{3}$$

where $\mathcal{L}$ is a linear operator. For a BiGlobal stability analysis, the three-dimensional perturbation is set to be spanwise homogeneous, $\tilde{\mathbf{u}}(x,y,z,t) = \hat{\mathbf{u}}(x,y)e^{i(\beta z-\omega t)} + c.c.$, where $\hat{\mathbf{u}}$ is the amplitude function, $\beta = 2\pi/L_z$ is the wavenumber along the spanwise periodic length L_z, and $c.c.$ is a complex conjugate to ensure that the perturbation is real valued. Here ω is the complex eigenvalue of the matrix $\mathcal{M}^{-1}\mathcal{L}$ of the equation:

$$\mathcal{L}\tilde{\mathbf{u}} = \omega\mathcal{M}\tilde{\mathbf{u}}, \tag{4}$$

which is derived from Eqn. (3). If $\Re\{\omega\} > 0$, the perturbation grows exponentially in time, producing an unstable flow. If $\Re\{\omega\} < 0$, the perturbation decays exponentially in time, producing a stable flow. If $\Re\{\omega\} = 0$, the flow is marginally stable.

As a complement to primary stability analysis, a secondary stability analysis based on Floquet theory [41] is performed in order to investigate the behavior of small-amplitude three-dimensional perturbations on a time-periodic base flow, $\bar{\mathbf{q}}(x, y, t) = \bar{\mathbf{q}}(x, y, t + T)$. In this analysis, Eqn. (2) contains a T-period operator $\mathcal{L}$ whose solution is of the form [42]:

$$\tilde{\mathbf{u}}(x, y, z, t) = \sum_{\beta=-\infty}^{\infty} \hat{\mathbf{u}}(x, y, t) e^{\sigma t} e^{i\beta z}, \tag{5}$$

where σ is a complex number. The stability of a time-periodic flow is determined by its Floquet multipliers, $|\mu| = e^{\sigma T}$. If $|\mu| > 1$, the perturbation grows, resulting in instability.

3. Numerical framework

3.1. Meshing

The computational domain has dimensions of $\Omega = \{x \in [-10, 25] \times y \in [0, 15]\}$ (in chord lengths). The mesh within it is discretized with *Gmsh* [43] into $O(2000)$ hybrid macro finite elements, as shown in Fig. 1(*left*). It is then exported to the open-source software *Nektar++* [44], which uses the spectral/hp method to solve partial differential equations. Around the airfoil, the grid resolution is increased by placing Gauss–Legendre–Lobatto nodes in each macro element, as shown in Fig. 1 (*right*) for a case with polynomial order $p = 8$. A detailed grid independence study is included in Appendix A.

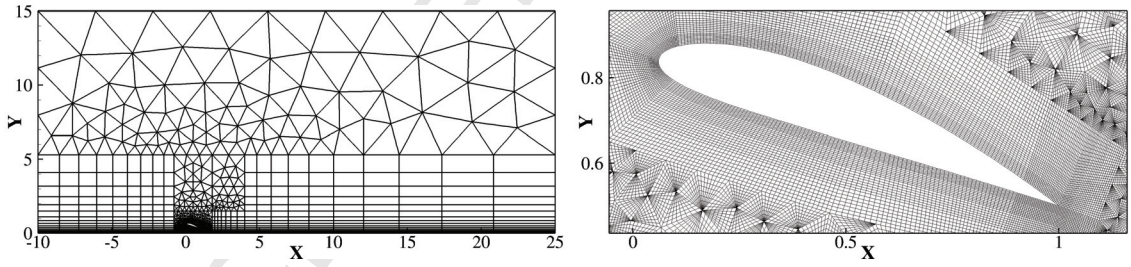

Fig. 1: (*left*) Full computational domain with macro elements shown and (*right*) a zoomed view of the Gauss–Legendre–Lobatto nodes around the airfoil as discretized with polynomial order $p = 8$.

3.2. Boundary conditions

As noted in Sec. 1.3, two realistic landing scenarios are considered. In the first scenario, an aircraft lands on a stationary runway in quiescent air, with zero relative air-to-ground velocity, implying the absence of a boundary layer. Here it is necessary for the boundary condition at the bottom of the computational domain to be a slip surface, referred to hereafter as a *slip ground*. In the second scenario, an aircraft lands on a moving runway (e.g.

an aircraft carrier), with non-zero relative air-to-ground velocity, implying the presence of a boundary layer. Here it is necessary for the boundary condition at the bottom of the computational domain to be a no-slip surface, referred to hereafter as a *no-slip ground*.

The first scenario (slip ground) is relatively easy to implement, but the second scenario (no-slip ground) requires additional considerations for the inlet boundary condition because of the boundary layer growing along the ground. Figure 2 shows the development of a boundary layer in front of and within the computational domain. The streamwise distance required for the boundary layer to grow along a non-inclined flat plate from a nominal upstream stagnation point to the location where the dimensionless thickness is $\delta = 1$ is defined as x_δ, but the actual development length available in the computational domain (i.e. the distance from the inlet to the airfoil) is just 10. It is therefore necessary to impose at the inlet ($x_0 \equiv x_\delta - 10$) an analytical Blasius profile with thickness δ_{x_0}, whose exact value depends on $Re \equiv U_\infty c/\nu$ and $Re_x \equiv U_\infty x_\delta/\nu$. The dimensionless Blasius boundary-layer thickness is defined as $\delta \approx 5.0x/\sqrt{Re_x}$, where the streamwise development distance is non-dimensionalized by the chord length. Table 1 summarizes the properties of the four different Blasius profiles used for the inlet boundary condition in this study.

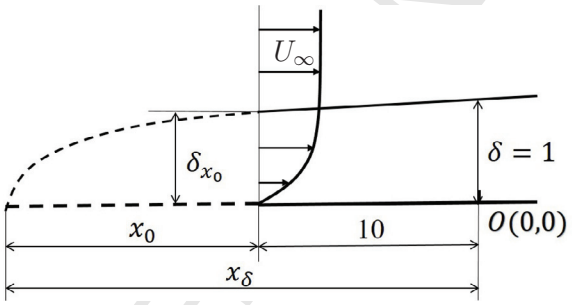

Fig. 2: Schematic of boundary-layer development in front of and within the computational domain.

Table 1: Properties of the Blasius profiles used for the inlet boundary condition.

Re	x_δ	x_0	δ_{x_0}	Re_x
300	12	2	0.41	3.6×10^3
500	20	10	0.71	1.0×10^4
800	32	22	0.83	2.56×10^4
1000	40	30	0.87	4.0×10^4

In the Blasius profile, v is much smaller than u but should not be ignored. Unlike in Ref. [15], where the v profile was modified to approach zero in the far field, we adopt a v profile that tends to a constant non-zero value outside the boundary layer. The u and v profiles imposed at the inlet boundary when $Re = 500$ are shown in Fig. 3. The pressure

at the inlet boundary is defined by a Neumann condition: $\partial p/\partial \mathbf{n} = 0$. The ground ($y = 0$) and the airfoil (NACA 4415) are defined as no-slip surfaces: $\mathbf{u} = 0$ and $\partial p/\partial \mathbf{n} = 0$. The remaining boundaries ($x = 25$, $y = 15$) are defined as outlets: $\partial \mathbf{u}/\partial \mathbf{n} = 0$ and $p = 0$. Throughout this study, a NACA 4415 airfoil is used, with its angle of attack kept constant at $\alpha = 20°$. Focusing on a two-dimensional (infinite span) airfoil, rather than a three-dimensional (finite span) wing, helps to simplify the flow geometry and stability analysis [45], without losing the salient features of the problem [38].

The boundary conditions for perturbations at the inlet and no-slip surfaces are:

$$\tilde{\mathbf{u}} = 0, \ \frac{\partial \tilde{p}}{\partial \mathbf{n}} = 0, \tag{6}$$

while the boundary conditions for perturbations at the outlet are:

$$\frac{\partial \tilde{\mathbf{u}}}{\partial \mathbf{n}} = 0, \ \tilde{p} = 0. \tag{7}$$

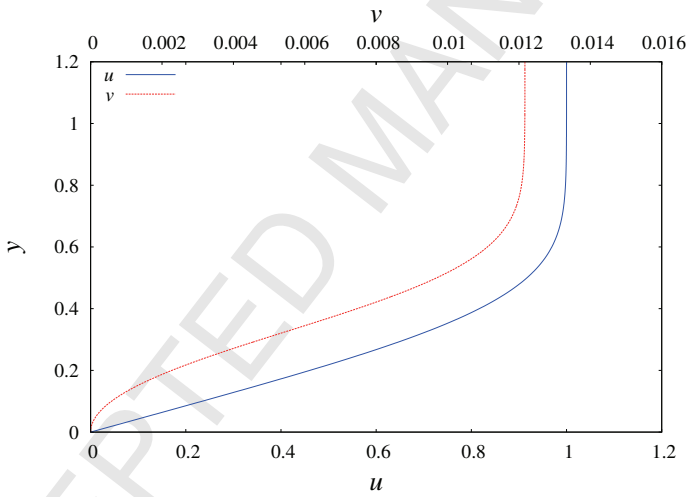

Fig. 3: Inlet boundary condition as defined by an analytical Blasius profile at $Re = 500$ (see Table 1).

4. Results and discussion

4.1. DNS of the wake dynamics

Direct numerical simulations (DNS) of the Navier–Stokes equations are performed in two dimensions to investigate the wake dynamics of a NACA 4415 airfoil at several values of Re and h but at a single angle of attack of $\alpha = 20°$. Because α is kept constant throughout this study, its value will not be mentioned again from here onwards. Figure 4 shows instantaneous snapshots of the spanwise vorticity distribution around the airfoil at $Re = 500$ for five different heights above a no-slip ground: $h = 0.2$, 0.3, 0.5, 0.8 and 1.0. These particular

values of h are chosen so as to place the airfoil at various heights within the boundary layer, where the strongest ground effect is expected. Here h is expressed in chord lengths and is measured from the airfoil's trailing edge. The properties of the boundary layer are listed in Table 1. For comparison, the case with no ground (i.e. without a solid surface at the bottom of the computational domain) is also shown: $h = \infty$.

When the airfoil is far from the ground (Fig. 4: $h \geqslant 0.8$), large-scale vortex shedding occurs after the flow separates from the leading and trailing edges, causing the wake to oscillate in a periodic limit cycle. This is confirmed by Fig. 5, which shows for $h = 0.8$ ($left$) a time trace of the instantaneous lift coefficient of the airfoil and ($right$) a phase portrait consisting of the u and v components of the local velocity sampled in the wake at (x, y) = (2.0, 1.0). The time trace shows periodic oscillations at a discrete natural frequency (see the inset of Fig. 5 for the frequency spectrum) and the phase portrait shows a closed repetitive trajectory, indicating that the wake oscillates periodically in a limit cycle. This behavior is characteristic of a globally unstable flow that acts as a self-excited hydrodynamic oscillator with intrinsic dynamics [46].

As the airfoil approaches the ground (as h decreases), the amplitude of the limit-cycle oscillations decreases (Fig. 4: $h = 0.5$) until the wake becomes steady (Fig. 4: $h \leqslant 0.3$). Thus, for a no-slip ground, reducing the ground clearance produces a stabilizing effect, weakening and then suppressing vortex shedding, causing the wake to transition from a self-excited hydrodynamic oscillator with an intrinsic natural frequency to a spatial amplifier of extrinsic perturbations [46]. Similar transitions have been observed before in low-density jets [47, 48, 49], cross-flowing jets [50], jet diffusion flames [51], thermoacoustic systems [52, 53, 54], and cylinder wakes [55]. It is worth mentioning that this stabilizing effect of the ground weakens with increasing Re. For example, for $h = 0.3$, the wake is steady at $Re = 500$ (Fig. 4) but is unsteady at $Re = 800$ (not shown). A more detailed study of the effect of Re will be presented in Sec. 4.3.2.

To further explore the wake dynamics of this airfoil–ground system, we show in Fig. 6 the Strouhal number $St \equiv fc/U_\infty$ as a function of h for three different Reynolds numbers: $Re =$ 500, 800 and 1000. Here f is the dominant frequency of the wake oscillations. We also show the normalized velocity amplitude $|u'/\bar{u}|$ sampled in the wake at (x, y) = (2.0, 1.0) for the same flow conditions. At $Re = 500$, as h increases from 0.2, $|u'/\bar{u}|$ starts off around zero but then increases in a square-root manner after h reaches a critical value (Hopf point), indicating a supercritical Hopf bifurcation to a global mode [46]. The onset of vortex shedding, which coincides with the Hopf point, occurs at $h = 0.30$–0.35. As Re increases, the critical h value decreases, showing again that the stabilizing effect of the ground weakens at higher Re. After the onset of vortex shedding, in the post-bifurcation regime, the St values for all three Reynolds numbers follow the same scaling, indicating that the length (c) and velocity (U_∞) scales used to define St here are capable of capturing the key flow physics.

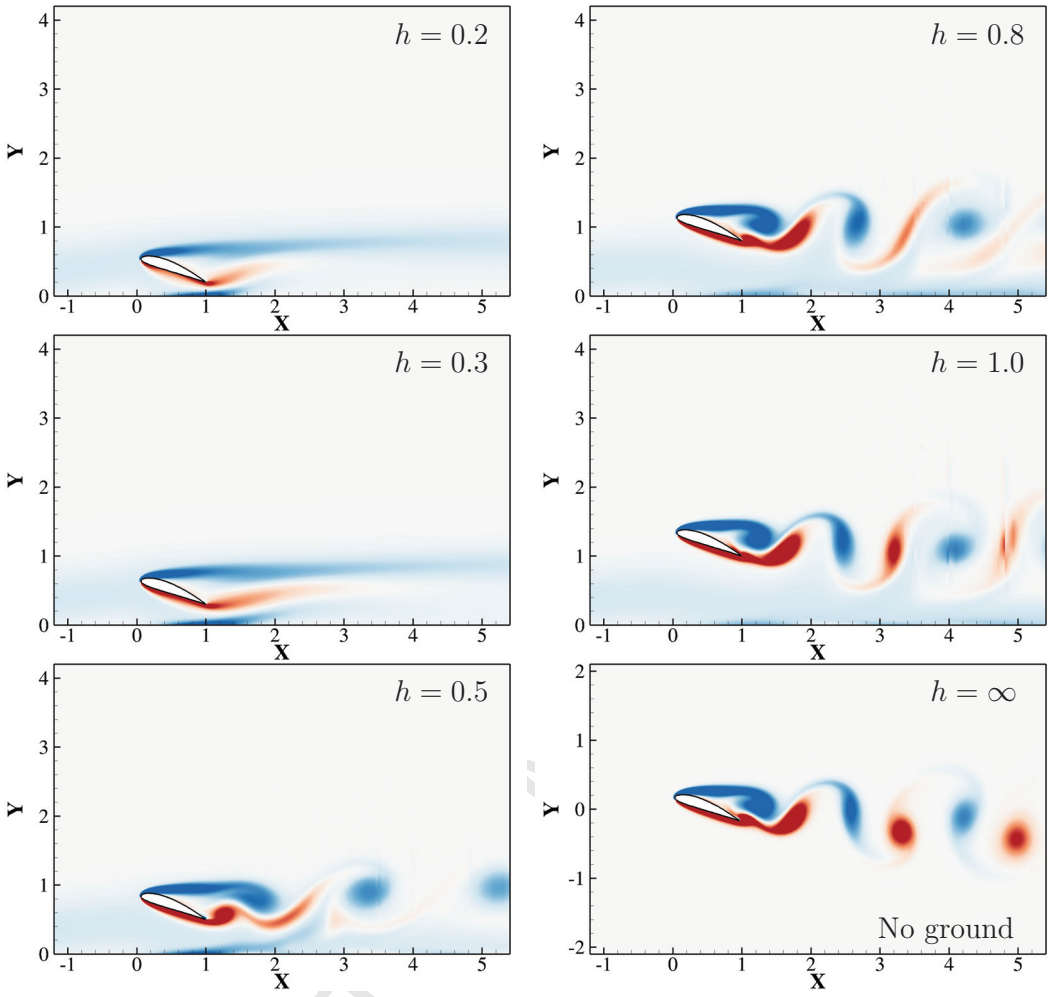

Fig. 4: DNS of the wake dynamics: instantaneous snapshots of the spanwise vorticity distribution around a NACA 4415 airfoil at $Re = 500$ for five different heights above a no-slip ground: $h = 0.2$, 0.3, 0.5, 0.8 and 1.0. For comparison, the case with no ground is also shown: $h = \infty$. The properties of the boundary layer are listed in Table 1. The colormap for the spanwise vorticity goes from $\omega_z = -5$ (blue) to $\omega_z = +5$ (red).

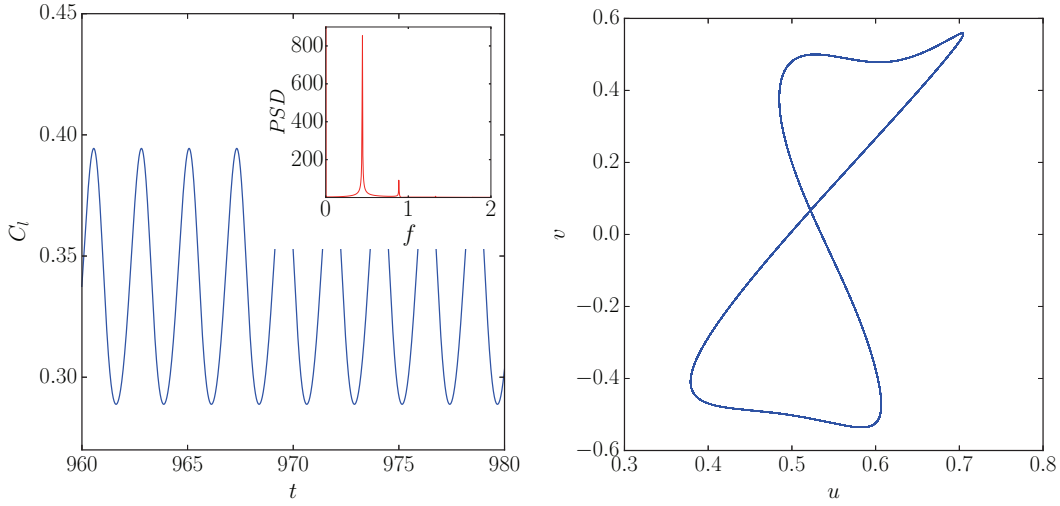

Fig. 5: Evidence of a limit cycle at $Re = 500$ and $h = 0.8$ for a no-slip ground: ($left$) a time trace of the instantaneous lift coefficient and ($right$) a phase portrait consisting of u and v sampled at $(x, y) = (2.0, 1.0)$.

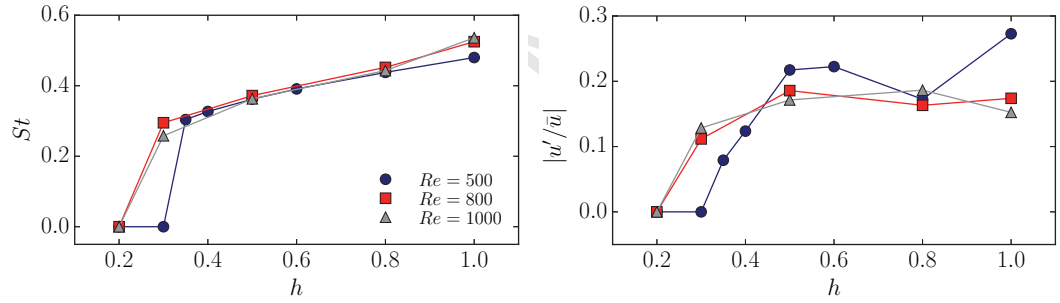

Fig. 6: Evidence of a Hopf bifurcation for a no-slip ground: ($left$) Strouhal number and ($right$) normalized velocity amplitude as a function of ground clearance for three different Reynolds numbers. The data are sampled in the wake at $(x, y) = (2.0, 1.0)$.

Figure 7 shows the time-averaged static pressure distribution $p(x)$ around the airfoil at different heights above a no-slip ground. At the leading edge, both the pressure and suction surfaces experience large spikes in p when $h \geqslant 0.8$, but p on the pressure surface gradually turns negative downstream of the mid-chord location, towards the trailing edge. There is no significant difference in the p distribution on the pressure surface when $h \geqslant 0.8$, but there is a small increase in p on the suction surface at $x \approx 0.7$ when $h = 0.8$, which, as we will see in Fig. 8, gives rise to a small drop in the lift coefficient. As the airfoil approaches the ground ($h < 0.8$), the magnitude of p on both the pressure and suction surfaces decreases markedly, resulting in a flatter p distribution. The area enclosed by the upper and lower p

curves is seen to decrease with decreasing h, which is consistent with the trends observed in the lift and drag coefficients for the case of a no-slip ground (Fig. 8).

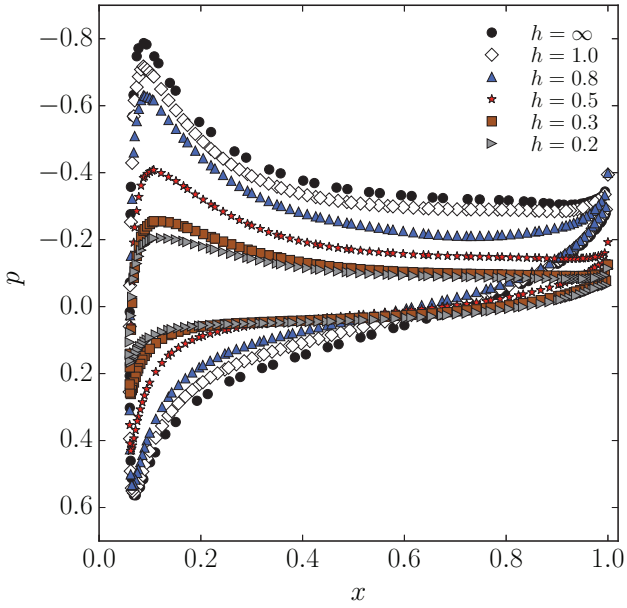

Fig. 7: Time-averaged static pressure distribution around the airfoil at $Re = 500$ for different heights above a no-slip ground.

Figure 8 shows the time-averaged drag coefficient (C_d) and lift coefficient (C_l) as a function of h for two different types of ground: a slip ground and a no-slip ground. For the slip ground (i.e. no boundary layer), which is the condition experienced by most aircraft landing on a stationary runway, decreasing h leads to an increase in pressure below the airfoil, increasing C_l. However, for the no-slip ground (i.e. with a boundary layer), decreasing h leads to a decrease in both C_d and C_l. This decrease is caused by the reduced velocities within the boundary layer, which reduce the lift and drag forces experienced by the airfoil. As is conventional, the coefficients C_d and C_l are defined here in terms of the free-stream velocity U_∞ (not the local velocity), which means that they are unable to account for the reduced velocities within the boundary layer. The effect of ground type on primary and secondary flow instabilities will be explored in Sec. 4.3.3 and Sec. 4.4.2.

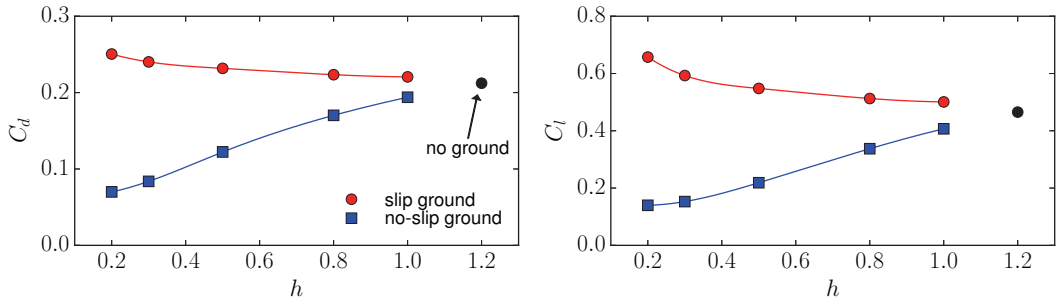

Fig. 8: (*left*) Drag coefficient and (*right*) lift coefficient as a function of ground clearance at $Re = 500$ for two different types of ground.

4.2. Computation of the steady base flow

For the analysis of primary instabilities (Sec. 4.3), it is necessary to obtain a steady-state solution of the base flow, even if that base flow may not be naturally steady. A proven way of doing this is to use selective frequency damping (SFD) [for details, see 56], which provides a means of filtering out the most unstable modes of the flow, yielding a steady but unstable solution to the Navier–Stokes equations:

$$\begin{cases} \dot{\mathbf{q}} = \mathbf{NS}(\mathbf{q}) - \chi(\mathbf{q} - \bar{\mathbf{q}}), \\ \dot{\bar{\mathbf{q}}} = (\mathbf{q} - \bar{\mathbf{q}})/\boldsymbol{\Delta}, \end{cases} \tag{8}$$

where χ is a positive control coefficient, Δ is the width of a first-order low-pass temporal filter, and $\dot{\mathbf{q}}$ and $\dot{\bar{\mathbf{q}}}$ are time-derivative quantities. Through a careful choice of χ and Δ, instabilities in the flow can be damped, producing a steady-state solution when $\mathbf{q} = \bar{\mathbf{q}}$.

Taking the $Re = 500$ case as an example, we perform SFD simulations on the unsteady flow at $h = 0.5$, 0.8, 1.0 and ∞; recall from Fig. 4 that the $h = 0.2$ and 0.3 cases are naturally steady. Figure 9 shows the steady but unstable solutions of the flow in the form of contour plots of the static pressure. For all six values of h, a large separation bubble can be seen forming immediately behind the suction surface of the airfoil, as evidenced by the large region of reverse flow (outlined by a black curve). As the airfoil approaches the ground ($h = \infty \to 0.2$), several observations can be made:

(i) The separation bubble decreases linearly in length L_b (Fig. 10), as measured downstream from the origin ($x = 0$), while the angle that its primary axis makes with the x-axis increases to a tip-up orientation. This is thought to occur because, as the airfoil becomes increasingly immersed in the viscous boundary layer, the flow around it slows down, reducing the speed of advection.

(ii) The long separation bubbles observed when $h \geqslant 0.5$ are unstable, with a natural tendency to oscillate about a mean state, even without turbulence in the free-stream.

(iii) The location of the separation point on the suction surface moves gradually downstream, away from the leading edge.

(iv) The static pressure distribution on both the pressure and suction surfaces decreases in magnitude and shifts towards the leading edge.

Collectively, these findings suggest that the geometrical changes occurring in the separation bubble are not due to changes in the effective width of the wake, but could be due to changes in the static pressure distribution on the suction surface of the airfoil.

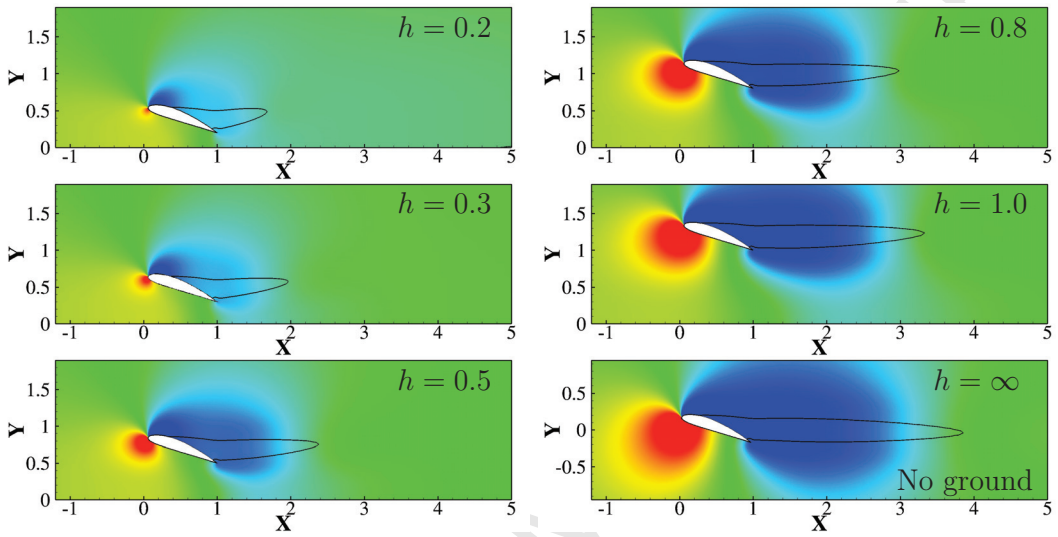

Fig. 9: Steady base-flow solutions for input into the primary stability analysis of Sec. 4.3: contours of the static pressure [(blue) $-1.5 \leqslant p \leqslant 1.5$ (red)] at $Re = 500$ for five different heights above a no-slip ground: $h = 0.2$, 0.3, 0.5, 0.8 and 1.0. For comparison, the case with no ground is also shown: $h = \infty$. The separation bubble is indicated by a region of reverse flow (outlined by a black curve).

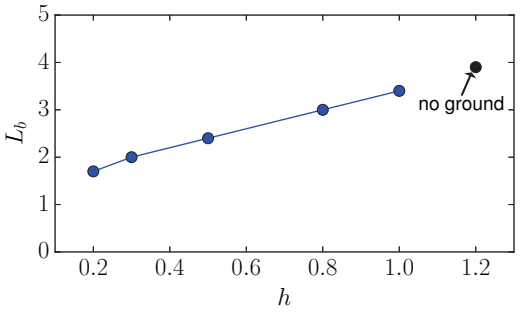

Fig. 10: Length of the separation bubble as a function of ground clearance at the conditions of Fig. 9.

4.3. Primary stability analysis

4.3.1. Effect of ground clearance

Figure 11 shows predictions from a primary stability analysis performed on the six base flows shown in Fig. 9. These flows are all at $Re = 500$ but at five different heights above a no-slip ground: $h = 0.2$, 0.3, 0.5, 0.8 and 1.0. For comparison, the case with no ground is also shown: $h = \infty$. Cases with a slip ground will be examined in Sec. 4.3.3.

An inspection of the growth rates reveals that the traveling modes (hollow markers) – referred to as the Kelvin–Helmholtz (KH) modes [27] – are the most unstable. By contrast, the stationary modes (solid markers) are less unstable/more stable, with higher spanwise wavenumbers (β). At $h = 0.2$ and 0.3, the perturbations in the range $\beta \in [0, 15]$ are all stable, decaying asymptotically with time. These perturbations are mostly stationary, except (i) at $h = 0.2$ with $\beta = 0.25$–0.5, where there are KH modes oscillating at low frequencies, and (ii) at $h = 0.3$ with $\beta = 0$–2, where there are KH modes oscillating at high frequencies.

The perturbations first become unstable at $h = 0.5$, starting with $\beta \approx 3.5$. This marginal-stability boundary is consistent with our DNS results showing that the wake transitions from a steady fixed point to an unsteady limit cycle at a critical ground clearance of $h = 0.30$–0.35 (Figs. 4 and 6). Unlike the steady cases ($h \leqslant 0.3$), the unsteady cases ($h \geqslant 0.5$) have unstable stationary modes dominating at $L_z \approx 1 \sim 2$ ($3 \leqslant \beta \leqslant 5$). The growth rates of these modes converge to a common decay as β increases above approximately 6. When the airfoil is near the edge of the boundary layer ($h = 0.8$–1.0), both the growth rate and St approach those of the case with no ground ($h = \infty$), indicating that the airfoil must be within the boundary layer in order for perturbations to be affected by the ground.

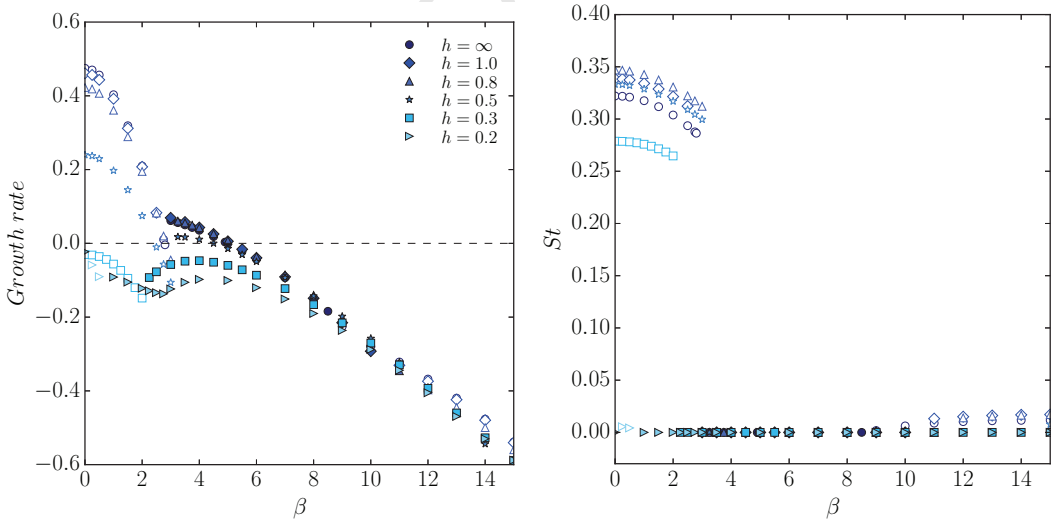

Fig. 11: Effect of ground clearance: modal stability analysis of the separated flow around a NACA 4415 airfoil at the flow conditions of Fig. 9: (*left*) growth rate and (*right*) Strouhal number, both as a function of the spanwise wavenumber. Hollow markers denote traveling modes; solid markers denote stationary modes.

Figure 12 shows the normalized amplitude function at $Re = 500$ and $h = 0.3$ for two different classes of modes: $(left)$ a traveling mode at $\beta = 1$ and $(right)$ a stationary mode at $\beta = 4$. The traveling mode, or KH mode, emerges first in the wake immediately behind the airfoil and then grows in the downstream direction. By contrast, the stationary mode, which is more damped than the KH mode, is dominated by its streamwise component $\hat{u}$, which is distributed throughout the wake region and within the boundary layer. Its spanwise component $\hat{w}$ is confined to the separation zone immediately behind the airfoil.

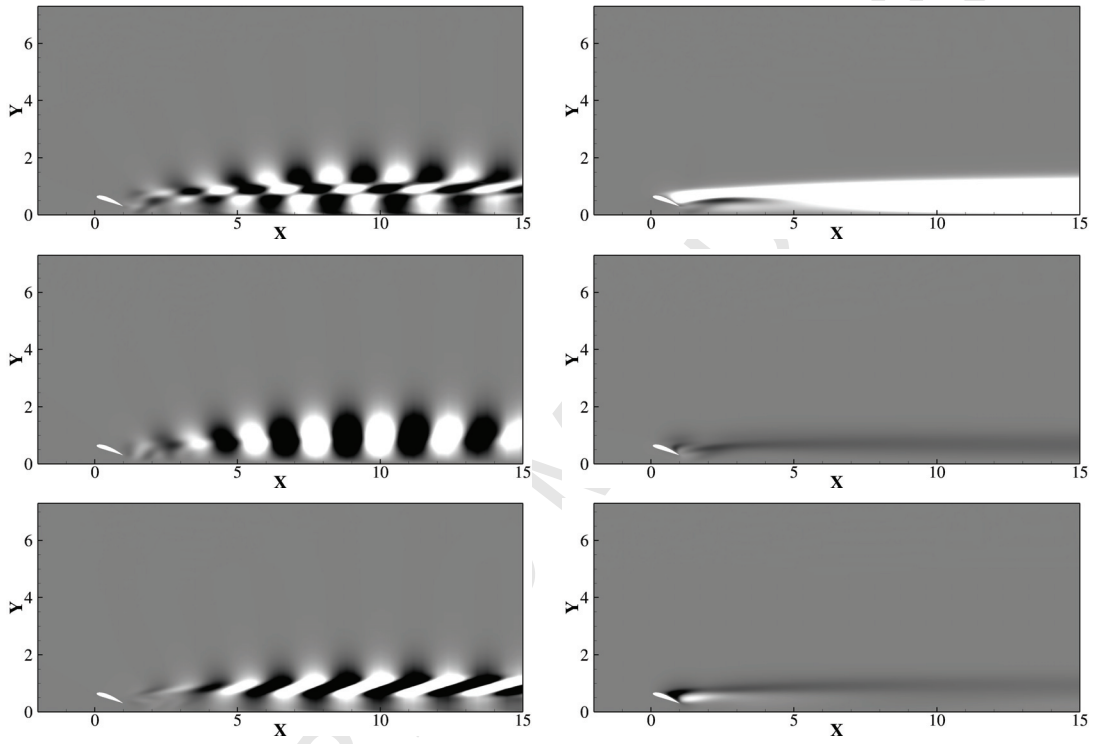

Fig. 12: Normalized amplitude function of the perturbations for $(left)$ a traveling mode at $\beta = 1$ and $(right)$ a stationary mode at $\beta = 4$. From top to bottom, the three perturbation components are $\hat{u}$, $\hat{v}$ and $\hat{w}$. The flow conditions are $Re = 500$ and $h = 0.3$. The gray-scale range is $-0.1 \leqslant \hat{u}, \hat{v}, \hat{w} \leqslant +0.1$

4.3.2. Effect of Reynolds number

To explore the effect of Re, we show in Fig. 13 predictions at $h = 0.5$ for three different Reynolds numbers: $Re = 500$, 800 and 1000. Although the boundary-layer thickness at the streamwise location of the airfoil is equal in all three cases, both the growth rate and frequency are seen to increase with Re. This increase is large when $Re = 500 \rightarrow 800$ but small when $Re = 800 \rightarrow 1000$, indicating that the destabilizing effect of Re weakens with increasing Re. It is worth noting that the range of β over which stationary modes arise shrinks with increasing Re. The predictions shown in Fig. 13 are for a no-slip ground but the qualitative trends also apply to the case of a slip ground (not shown).

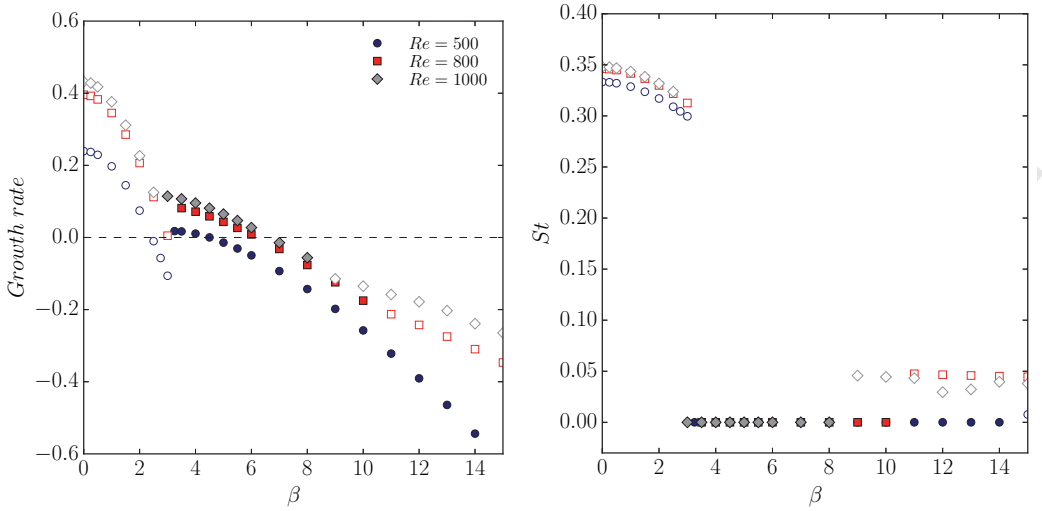

Fig. 13: Effect of Re: modal stability analysis of the separated flow around a NACA 4415 airfoil at $h = 0.5$ for three different Reynolds numbers and a no-slip ground. (*left*) Growth rate and (*right*) Strouhal number, both as a function of the spanwise wavenumber. Hollow markers denote traveling modes; solid markers denote stationary modes.

Figure 14 is analogous to Fig. 11 but at a higher Re of 800 (vs $Re = 500$). As with our earlier observations, the growth rates at $Re = 800$ are higher and decay more slowly than those at $Re = 500$. Between $h = 0.8$ and 1.0, the predictions are similar, indicating again that the effect of the ground is limited to within the boundary layer.

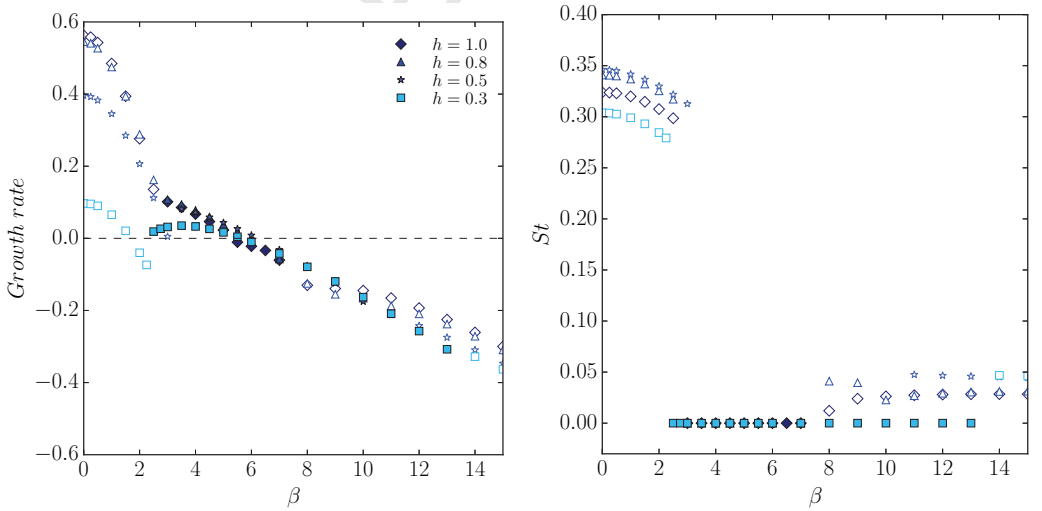

Fig. 14: The same as for Fig. 11 but at a higher Reynolds number: $Re = 800$.

4.3.3. Effect of ground type: no-slip vs slip

Switching from a no-slip ground (with a boundary layer defined by the Blasius profiles of Table 1) to a slip ground (without a boundary layer) results in a more unstable wake. This can be seen in the DNS results of Fig. 15, which compares the vorticity distribution between the two types of ground at $Re = 300$ and $h = 0.5$. It can also be seen in the instability analysis of Fig. 16, which shows that the slip ground does indeed produce the highest growth rates across the entire range of β examined. This destabilizing effect of the slip ground occurs because the removal of the boundary layer enables the velocity near the ground to increase to that of the free-stream, increasing the velocity experienced by the airfoil when $h < 1$. Thus, switching from a no-slip ground to a slip ground is akin to increasing Re, producing a similar destabilizing effect on the separated flow.

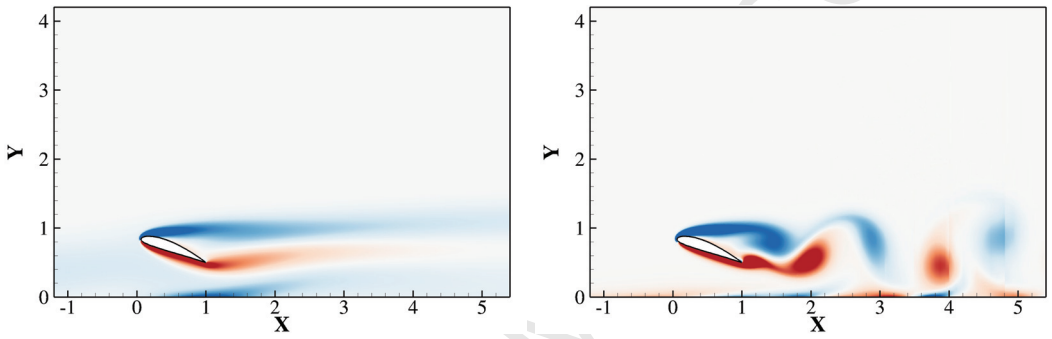

Fig. 15: Vorticity distribution at $Re = 300$ and $h = 0.5$ for two different types of ground: ($left$) a no-slip ground and ($right$) a slip ground.

Compared with the no-ground case, a slip ground is destabilizing but a no-slip ground is stabilizing. However, there is no significant difference in frequency between a slip ground and no ground, with both cases producing a higher St than a no-slip ground. For all three types of ground, the transition from a traveling mode (hollow markers) to a stationary mode (solid markers) occurs at approximately the same spanwise wavenumber: $\beta \approx 2.5$. For a no-slip ground, the particular flow condition shown in Fig. 16 ($Re = 300$, $h = 0.5$) is at the marginal-stability boundary ($\beta = 0$) for the onset of vortex shedding.

In summary, introducing a slip ground to an otherwise groundless system is destabilizing but introducing a no-slip ground is stabilizing. This shows that, depending on its specific type, the ground can have different effects on the primary stability of the separated flow around an airfoil at low Re.

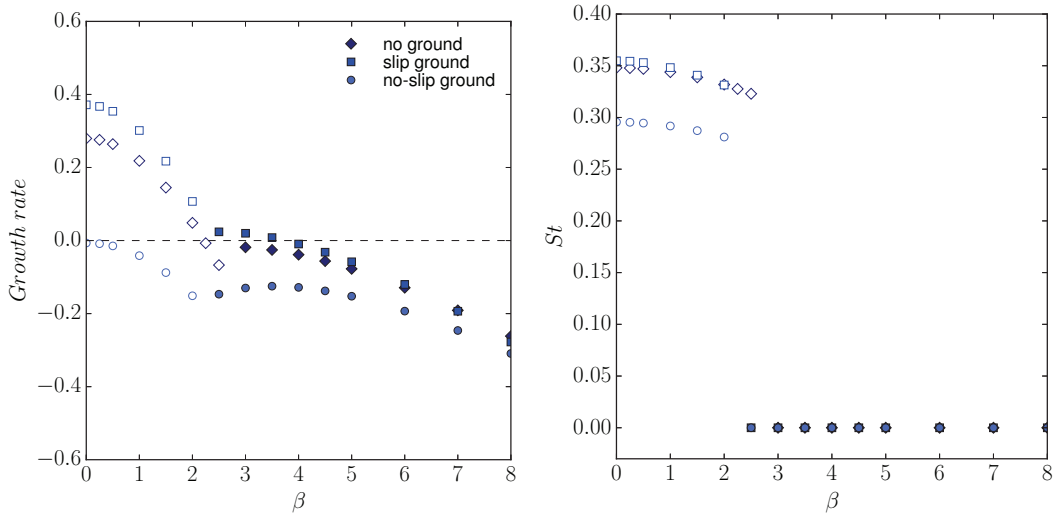

Fig. 16: Effect of ground type: modal stability analysis of the separated flow around a NACA 4415 airfoil at $Re = 300$ and $h = 0.5$ for three different types of ground: no ground, slip ground, and no-slip ground. ($left$) Growth rate and ($right$) Strouhal number, both as a function of the spanwise wavenumber. Hollow markers denote traveling modes; solid markers denote stationary modes.

4.3.4. Effect of the input base state: SFD vs time averaging

To assess the sensitivity of the stability analysis to the input base state, we compare in Fig. 17 predictions from two different types of base states: one computed with selective frequency damping (SFD) and one computed with time averaging. These were introduced in Sec. 4.2. There are many similarities but also some important differences between the two methods. Both predict that the two most dominant modes are the traveling and stationary modes. However, the time-averaging method predicts these to be stable across the full range of spanwise wavenumbers considered, whereas the SFD method predicts both the traveling and stationary modes to be unstable. From the DNS results of Fig. 4, which are obtained at the same conditions as Fig. 17, the flow can be seen to oscillate periodically in a limit cycle, indicating that the SFD method is more accurate than the time-averaging method when it comes to predicting the growth rate of perturbations. A similar conclusion has been reached before in the analysis of cylinder wakes [57] and the flow around a NACA 0015 airfoil at $Re = 1000$ [30]. Nevertheless, the Strouhal number shows relatively little difference between the two methods. For the most dominant mode, the SFD method gives $St = 0.333$ while the time-averaging method gives $St = 0.359$; these predictions are within 8% of the DNS value of $St = 0.361$. Given that the time-averaged base flow can be computed relatively quickly and cheaply, it could be argued that the time-averaging method is acceptable for situations in which only frequency predictions are required. However, if the situation calls for accurate predictions of the growth rate as well, the SFD method should be used.

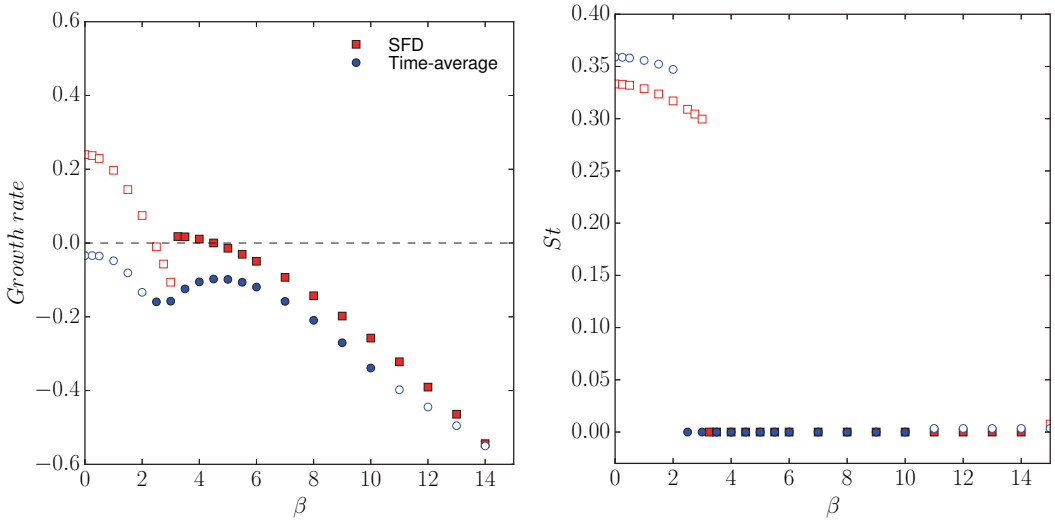

Fig. 17: Effect of the input base state: modal stability analysis of the separated flow around a NACA 4415 airfoil at $Re = 500$ and $h = 0.5$ for two different types of base states: one computed with SFD and one computed with time averaging. (*left*) Growth rate and (*right*) Strouhal number, both as a function of the spanwise wavenumber. Hollow markers denote traveling modes; solid markers denote stationary modes.

4.4. Secondary stability analysis

We perform a Floquet analysis to investigate the stability of three-dimensional perturbations on a time-periodic base flow computed with two-dimensional DNS. Care is taken to ensure that the flow settles into a saturated limit cycle with a nominally fixed amplitude and frequency, by monitoring the evolution of the lift and drag coefficients at several locations within the flow. The integration of Eqn. 5 requires a phase-averaged flow, which we obtain from 32 discretized slices of one oscillation period of the two-dimensional base flow.

Figure 18 shows the Floquet multiplier (μ) at $Re = 500$ for three different heights above a no-slip ground ($h = 0.5, 0.8, 1.0$) and for the case with no ground ($h = \infty$). Starting with the no-ground case ($h = \infty$), we find two crests in the perturbation curve. The crest at $\beta \approx 3$ is the so-called long-wavelength (LW) mode, which is very close to the critical wavenumber [27] but is stable ($\mu < 1$). By contrast, the crest at $\beta \approx 11$ is the so-called short-wavelength (SW) mode, which is unstable with μ peaking at around 1.5, indicating a secondary bifurcation of the time-periodic base flow.

As the airfoil approaches the ground ($h = \infty \rightarrow 1.0$), the SW mode ($\beta \approx 11$) becomes less unstable, while the LW mode ($\beta \approx 3$) becomes less stable (even bordering on slightly unstable), although the amplitude of the LW mode is still much smaller than that of the SW mode. Closer to the ground ($h = 0.8$), the SW mode ($\beta \approx 11$) continues to weaken, becoming stable ($\mu < 1$), while the LW mode ($\beta \approx 3$) remains close to the marginal-stability boundary ($\mu = 1.0009$). Closer to the ground still ($h = 0.5$), the SW mode ($\beta \approx 9.5$) is now significantly more stable than the LW mode ($\beta \approx 4.5$), which has shifted to a slightly higher spanwise wavenumber and has weakened in amplitude ($\mu < 1$), indicating the absence of

secondary instabilities. This shows that a no-slip ground can have a stabilizing effect on secondary instabilities – much as it does on primary instabilities (Sec. 4.3).

Figure 19 shows contours of the spanwise vorticity amplitude function for the LW mode ($\beta \approx 3$) and the SW mode ($\beta \approx 11$) at $Re = 500$ and $h = 1.0$ with a no-slip ground. In the LW mode (Fig. 19 *left*), the vortices shed behind the airfoil interact strongly with the developing boundary layer, especially after five chord lengths from the airfoil. This interaction causes the initially coherent wake structures to merge together, becoming distorted. In the SW mode (Fig. 19 *right*), the vorticity distribution is particularly strong near the trailing edge, covering around one quarter-chord of the suction surface. However, this SW perturbation decays more rapidly in the streamwise direction than the LW perturbation does, nearly vanishing by around five chord lengths from the airfoil, even though the SW mode has a higher maximum amplitude than the LW mode. This shows that although the SW mode is more unstable than the LW mode, its effect is limited to a relatively small region behind the airfoil, whereas the effect of the LW mode persists farther downstream.

In the boundary layer along a flat plate, the flow starts off as being laminar, then enters a transition regime above a critical Re_x, and eventually becomes turbulent at a higher Re_x. The natural transitional Reynolds number is typically $Re_x = 3.9 \times 10^6$ [58], which is two orders of magnitude higher than the maximum Re_x found in our study ($Re_x = 7.5 \times 10^4$), which occurs at the downstream end of our computational domain. This shows that the distorted structures seen in Fig. 19 (*left*) are caused by an inherent feature of the LW mode, not by transition in the boundary layer.

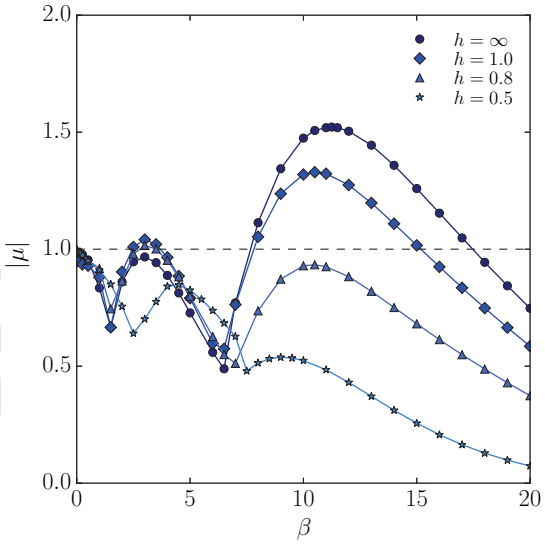

Fig. 18: Secondary instability analysis: Floquet multiplier as a function of the spanwise wavenumber at $Re = 500$ for three different heights above a no-slip ground and the case with no ground: $h = 0.5$, 0.8, 1.0 and ∞.

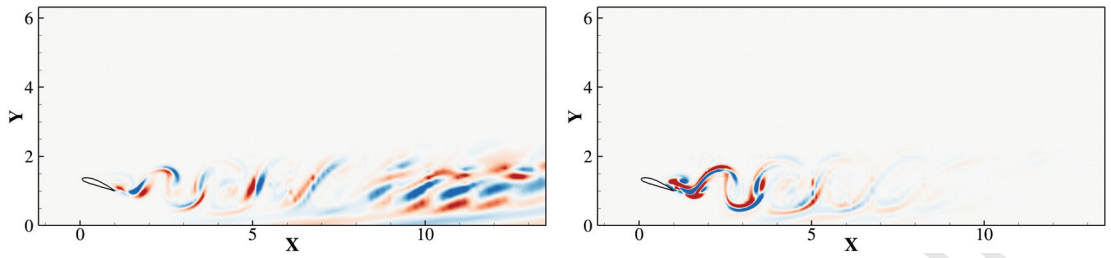

Fig. 19: Spanwise vorticity amplitude function ($\hat{\omega}_z$) of two Floquet modes at $Re = 500$ and $h = 1.0$ with a no-slip ground: ($left$) LW mode at $\beta \approx 3$ and ($right$) SW mode at $\beta \approx 11$.

4.4.1. Stall cells

In linear stability analysis, the total flow field can be reconstructed by superimposing small-amplitude perturbations onto the base flow. This is shown in Fig. 20, with the surface streamlines shown in Fig. 21. For both the LW mode ($\beta \approx 3$) and the SW mode ($\beta \approx 11$), the streamwise and spanwise vorticities are visualized three-dimensionally via multiplication with the amplitude $\epsilon = 5 \times 10^{-4}$.

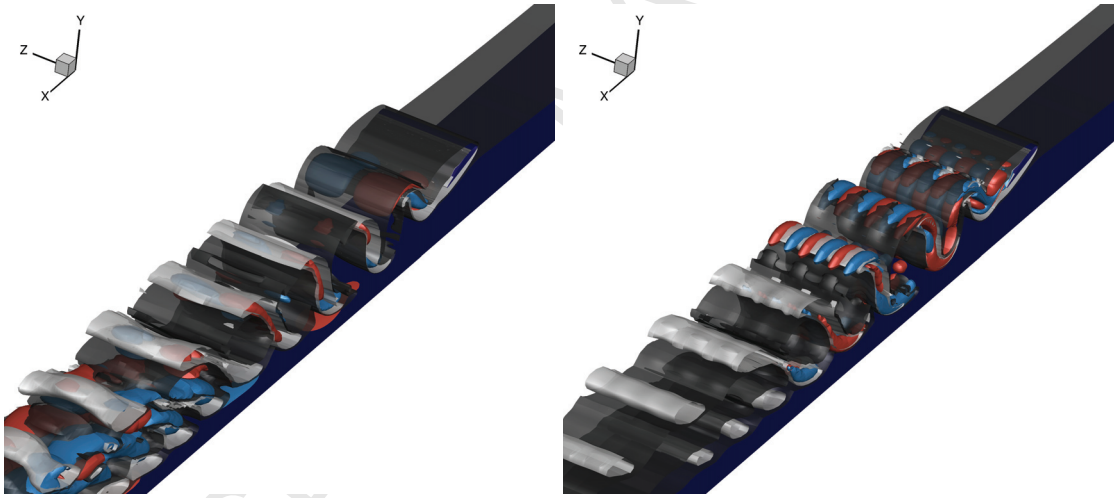

Fig. 20: Three-dimensional reconstruction of Fig. 19 via a superposition of two periods of the secondary perturbation onto the time-periodic base flow: ($left$) LW mode at $\beta \approx 3$ and ($right$) SW mode at $\beta \approx 11$. The blue-red hues show the streamwise vorticity, the black-white tones show the spanwise vorticity, and the navy background shows the airfoil and the no-slip ground.

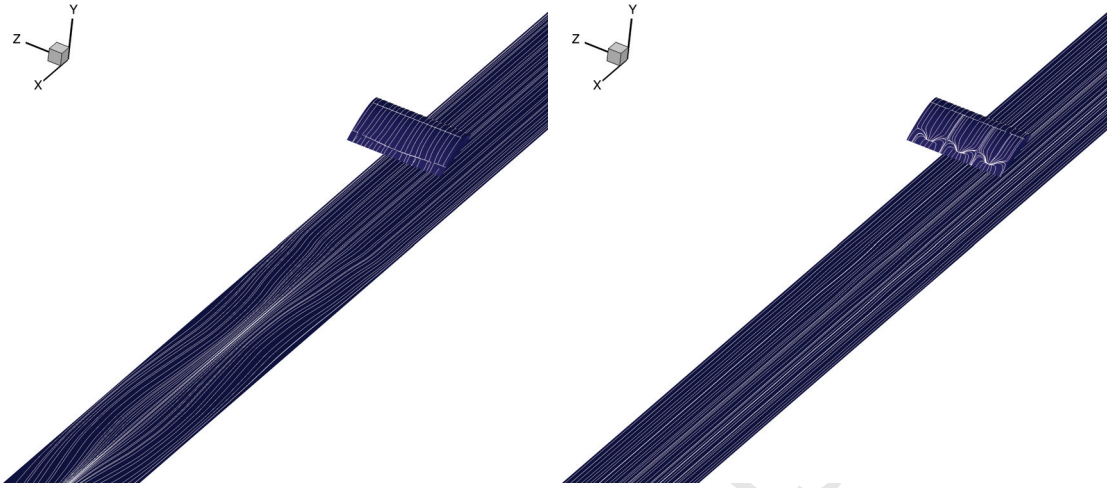

Fig. 21: Surface streamlines of Fig. 20: ($left$) LW mode at $\beta \approx 3$ and ($right$) SW mode at $\beta \approx 11$.

For the SW mode ($\beta \approx 11$), there are stall cells on the upper surface of the airfoil with a wavelength of $L_z = 6\pi/11$. In a previous study [27], similar stall cells were found in the flow around an airfoil without a ground. The fact that we find stall cells here shows that the ground does not have a major influence on the formation of stall cells. For the LW mode ($\beta \approx 3$), there are no stall cells, but the wake behind the airfoil is still perturbed, particularly along the ground.

For both the SW and LW modes, Fig. 21 shows that the streamlines ahead of the airfoil run parallel to the free-stream. Behind the airfoil, the streamlines near the ground surface of the LW mode converge and then diverge with downstream development, whereas those of the SW mode remain parallel to the free-stream.

4.4.2. Effect of ground type: no-slip vs slip

Figure 22 explores the effect of ground type on secondary instabilities at $Re = 500$ and $h = 0.8$. The LW mode ($\beta \approx 3$) is relatively insensitive to ground type, but the SW mode ($\beta \approx 11$) is not: it is stable with a no-slip ground, unstable with no ground, and the most unstable with a slip ground. Therefore, similar to what we observed in our analysis of primary instabilities (Sec. 4.3.3), introducing a slip ground to an otherwise groundless system is destabilizing but introducing a no-slip ground is stabilizing. This is thought to occur because a slip ground increases the velocity under the airfoil, increasing the local shear and thus amplifying the instability. By contrast, a no-slip ground decreases the velocity under the airfoil, decreasing the local shear and thus weakening the instability. These results show that, depending on its specific type, the ground can have differing effects on the secondary stability of the separated flow around an airfoil at low Re.

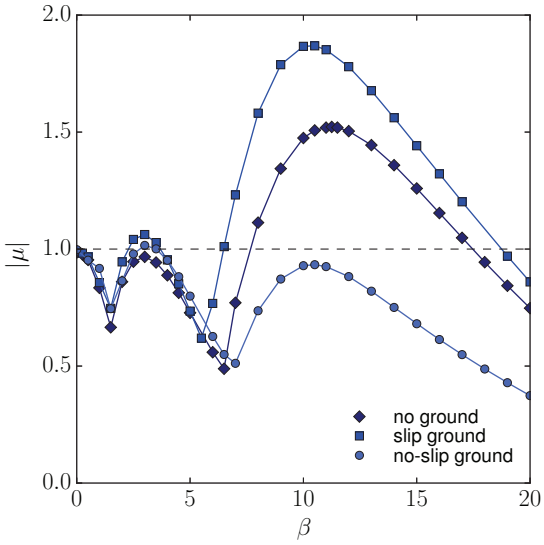

Fig. 22: Effect of ground type on secondary instabilities at $Re = 500$ and $h = 0.8$.

5. Conclusions

In this numerical–theoretical study, we have performed a linear BiGlobal modal stability analysis on the separated flow around a NACA 4415 airfoil at low Reynolds numbers ($Re =$ 300–1000) and a high angle of attack ($\alpha = 20°$), with a focus on the effect of the airfoil's proximity to two different types of ground: (i) a stationary ground, which is used to simulate an aircraft landing on a stationary runway and is modeled as a *slip ground* without a boundary layer, and (ii) a moving ground, which is used to simulate an aircraft landing on a moving runway (e.g. an aircraft carrier) and is modeled as a *no-slip ground* with a boundary layer defined analytically by the Blasius profile.

The most dominant perturbation was found to be a traveling mode of the Kelvin–Helmholtz type, which gives rise to a supercritical Hopf bifurcation to global instability, resulting in a periodic limit cycle in the form of large-scale vortex shedding behind the airfoil. As the clearance between the airfoil and the ground decreases, this mode can become more unstable or less unstable, depending on the specific type of ground present: introducing a slip ground (stationary ground) to an otherwise groundless system is destabilizing but introducing a no-slip ground (moving ground) is stabilizing, although both effects weaken with increasing Re. By performing a Floquet analysis, we found that short-wavelength secondary instabilities are damped by a no-slip ground but are amplified by a slip ground. By contrast, long-wavelength secondary instabilities are relatively insensitive to ground type. This study shows that the ground can have an elaborate influence on the primary and secondary instabilities of the separated flow around an airfoil at low Re. These findings could have important implications for the design of micro aerial vehicles and for the understanding of natural flyers such as insects and birds.

Acknowledgements

This work was supported by the Research Grants Council of Hong Kong (Project No. 16235716 and 26202815). WH would like to acknowledge the support provided by the China Scholarship Council during his studies in Madrid. PY would like to thank the Special Program for Applied Research on Super Computation of the NSFC-Guangdong Joint Fund (second phase) under Grant No. U1501501.

Appendix A. Demonstration of grid independence

To confirm the grid independence of mesh $M1$ in Fig. 1, we perform a two-step procedure as per Refs. [35, 27]:

1. We incrementally increase the polynomial order p in the spectral/hp code. Table A.2 shows the force coefficients (C_d and C_l) and vorticity (ω_z) sampled at a location in the wake, $(x, y) = (3, 0.5)$, for several values of p. It is clear that, as long as $p \geqslant 8$, ω_z is accurate to four decimal places.
2. We examine the density of the discretized elements in the computational domain. We double the element density in the wake region behind the airfoil in order to build a new mesh, $M2$. A recalculation of the vorticity at the location $(x, y) = (3, 0.5)$ with $p = 8$ gives $\omega_z = 0.385968$, which is almost identical (to five decimal places) to the value obtained with mesh $M1$, $\omega_z = 0.385965$. Balancing computational efficiency and cost, we use mesh $M1$ and $p = 8$ in our base-flow simulations and stability analysis.

To further validate the mesh quality, we perform a sensitivity analysis. Table A.3 compares the direct and adjoint modes of the two-dimensional flow at $Re = 500$, $\alpha = 20°$ and $h = 0.3$. The two modes are nearly identical (to three decimal places), indicating that the computational domain is large enough to have no significant influence on the stability of the computed flow. The vorticity distribution of these direct and adjoint modes are shown in Fig. A.23. The adjoint analysis shows a zone of strong sensitivity around the airfoil, with the wake region containing perturbations that resemble braid-like convective modes.

Table A.2: Grid independence study, where the error is based on ω_z in mesh $M1$.

p	C_d	C_l	ω_z	Error (%)
5	0.08372	0.15278	0.387149	0.1550
6	0.08374	0.15386	0.386365	0.0366
7	0.08376	0.15280	0.386333	0.0334
8	0.08377	0.15279	0.385965	0.0034
9	0.08378	0.15281	0.385986	0.0013
10	0.08379	0.15282	0.385999	–

Table A.3: Global stability analysis of the flow at $Re = 500$ and $h = 0.3$ with $\beta = 0$.

	ω_r	ω_i
Direct mode	-0.0304	1.7517
Adjoint mode	-0.0307	1.7516

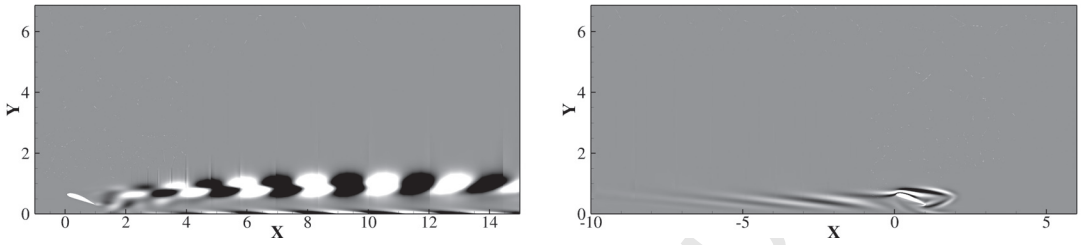

Fig. A.23: Vorticity distribution of the ($left$) direct and ($right$) adjoint modes at $Re = 500$ and $h = 0.3$ with $\beta = 0$.

References

[1] Q. Qu, X. Jia, W. Wang, P. Liu, R. K. Agarwal, Numerical study of the aerodynamics of a NACA 4412 airfoil in dynamic ground effect, Aerosp. Sci. Technol. 38 (2014) 56–63.

[2] M. Halloran, S. O'Meara, Wing in ground effect craft review, Tech. Rep. DSTO-GD-0201, DSTO (Australia), 1999.

[3] K. V. Rozhdestvensky, Wing-in-ground effect vehicles, Prog. Aerosp. Sci. 42 (3) (2006) 211–283.

[4] M. T. Dakhrabadi, M. Seif, Influence of main and outer wings on aerodynamic characteristics of compound wing-in-ground effect, Aerosp. Sci. Technol. 55 (2016) 177–188.

[5] Y. J. Moon, H. Oh, J. Seo, Aerodynamic investigation of three-dimensional wings in ground effect for aero-levitation electric vehicle, Aerosp. Sci. Technol. 9 (6) (2005) 485–494.

[6] J. Li, G. Lei, Y. Xian, X. Wang, Research on Ground Effect of Shipborne Flying-Wing UAV, in: 2014 Tenth International Conference on Computational Intelligence and Security, 685–688, 2014.

[7] Q. Qu, R. K. Agarwal, Chord-dominated Ground-effect Aerodynamics of Fixed-wing UAVs, John Wiley & Sons, Ltd, 201–254, 2017.

[8] J. Wu, C. Shu, N. Zhao, W. Yan, Fluid Dynamics of Flapping Insect Wing in Ground Effect, J. Bionic Eng. 11 (1) (2014) 52–60.

[9] D. Kolomenskiy, M. Maeda, T. Engels, H. Liu, K. Schneider, J.-C. Nave, Aerodynamic Ground Effect in Fruitfly Sized Insect Takeoff, PLoS ONE 11 (3) (2016) 1–21.

[10] H. Lu, K. B. Lua, T. T. Lim, K. S. Yeo, Ground effect on the aerodynamics of three-dimensional hovering wings, Bioinspir. Biomim. 11 (2016) 066003.

[11] M. R. Ahmed, T. Takasaki, Y. Kohama, Aerodynamics of a NACA 4412 airfoil in ground effect, AIAA J. 45 (1) (2007) 37–47.

[12] W. Yang, C. Ying, Z. Yang, Aerodynamics study of WIG craft near curved ground, J. Hydrodyn. Ser. B 22 (5) (2010) 371–376.

[13] T. Gao, N. Liu, X. Lu, Numerical analysis of the ground effect on insect hovering, J. Hydrodyn. Ser. B 20 (1) (2008) 17–22.

[14] C. Zhang, H. Huang, X. Lu, Free Locomotion of a flexible plate near the ground, Phys. Fluids 29 (2017) 041903.

[15] Z. Li, C. Lan, L. Jia, Y. Ma, Ground effects on separated laminar flows past an inclined flat plate, Theor. Comput. Fluid Dyn. 31 (2) (2017) 127–136.
[16] Z. Yang, W. Yang, Q. Jia, Ground Viscous Effect on 2D Flow of Wing in Ground Proximity, Eng. App. Comp. Fluid 4 (4) (2010) 521–531.
[17] K. Taira, T. Colonius, Three-dimensional flows around low-aspect-ratio flat-plate wings at low Reynolds numbers, J. Fluid Mech. 623 (2009) 187–207.
[18] P. Freymuth, F. Finaish, W. Bank, Further visualization of combined wing tip and starting vortex systems, AIAA J. 25 (9) (1987) 1153–1159.
[19] W. Yang, Z. Yang, Schemed Power-augmented Flow for Wing-in-ground Effect Craft in Cruise, Chinese J. Aeronaut. 24 (2) (2011) 119–126.
[20] Y. Qin, P. Liu, Q. Qu, T. Hu, Wing/canard interference of a close-coupled canard configuration in static ground effect, Aerosp. Sci. Technol. 69 (2017) 60–75.
[21] V. Theofilis, S. J. Sherwin, Global instabilities in trailing- edge laminar separated flow on a NACA 0012 aerofoil, in: Proceedings of the XV International Symposium on Airbreathing Engines ISABE 2001-1094, Bangalore, India, September 3-7, 2001, 2001.
[22] V. Theofilis, D. Barkley, S. Sherwin, Spectral/hp element technology for global flow instability and control, Aeronaut. J.(1968) 106 (1065) (2002) 619–625.
[23] S. A. Loh, H. M. Blackburn, S. J. Sherwin, Transient growth in an airfoil separation bubble, in: 19th Australasian Fluid Mechanics Conference, Melbourne, Australia, Dec 8-11, 2014, 2014.
[24] V. Kitsios, D. Rodríguez, V. Theofilis, A. Ooi, J. Soria, BiGlobal stability analysis in curvilinear coordinates of massively separated lifting bodies, J. Comp. Phys. 228 (2009) 7181–7196.
[25] D. Rodríguez, V. Theofilis, On the birth of stall cells on airfoils, Theor. Comput. Fluid Dyn. 25 (2011) 105–117.
[26] R. S. Gioria, W. He, V. Theofilis, On Global Linear Instability Mechanisms of Flow Around Airfoils at Low Reynolds Number and High Angle of Attack, Procedia IUTAM 14 (2015) 88–95.
[27] W. He, R. S. Gioria, J. M. Pérez, V. Theofilis, Linear instability of low Reynolds number massively separated flow around three NACA airfoils, J. Fluid Mech. 811 (2017) 701–741.
[28] W. Zhang, R. Samtaney, BiGlobal linear stability analysis on low-Re flow past an airfoil at high angle of attack, Phys. Fluids 28 (2016) 044105.
[29] S. P. Tsiloufas, R. S. Gioria, J. R. Meneghini, Floquet stability analysis of the flow around an airfoil, in: 20th International Congress of Mechanical Engineering, Gramado, RS, Brazil, November 15-20, 2009, 2009.
[30] C. Brehm, H. F. Fasel, BiGlobal Stability Analysis as an Initial Value Problem for a Stalled Airfoil, in: 41st AIAA Fluid Dynamics Conference and Exhibit Honolulu, Hawaii, AIAA Paper 2011–3569, 2011.
[31] J. S. Humphreys, On a circular cylinder in a steady wind at transition Reynolds numbers, J. Fluid Mech. 9 (1960) 603–612.
[32] G. B., Experimentelle Untersuchungen des laminaren-turbulenten überganges der Zylindergrenzschicht-stroemung, Tech. Rep. 2001-14, DLR Institut fuer Aerodynamik und Strömungstechnikt, 2001.
[33] B. H., T. M., Windkanalmessungen in einem Rechteckflügel bei anliegender und abgelöster Strömung, Tech. Rep. IB251-80A18, DFVLR Forschungsbericht, 1980.
[34] G. Schewe, Reynolds-number effects in flow around more-or-less bluff bodies, J. Wind Eng. Ind. Aerodyn. 89 (2001) 1267–1289.
[35] N. Abdessemed, S. J. Sherwin, V. Theofilis, Linear instability analysis of low pressure turbine flows, J. Fluid Mech. 628 (2009) 57–83.
[36] A. Sharma, N. Abdessemed, S. J. Sherwin, V. Theofilis, Transient growth mechanisms of low Reynolds number flow over a low-pressure turbine blade, Theor. Comp. Fluid Dyn. 25 (2011) 19–30.
[37] G. Rocco, T. Zaki, X. Mao, H. Blackburn, S. Sherwin, Floquet and transient growth stability analysis of a flow through a compressor passage, Aerosp. Sci. Technol. 44 (2015) 116–124, Instability and Control of Massively Separated Flows.
[38] W. He, J. Á. Tendero, P. Paredes, V. Theofilis, Linear instability in the wake of an elliptic wing, Theor. Comput. Fluid Dyn. doi:10.1007/s00162-016-0400-2.

[39] V. Theofilis, Advances in global linear instability of nonparallel and three-dimensional flows, Prog. Aerosp. Sci. 39 (4) (2003) 249–315.
[40] V. Theofilis, Global linear instability, Annu. Rev. Fluid Mech. 43 (2011) 319–352.
[41] T. Herbert, Secondary Instability of Boundary Layers, Annu. Rev. Fluid Mech. 20 (1988) 487–526.
[42] D. Barkley, R. D. Henderson, Three-dimensional Floquet stability analysis of the wake of a circular cylinder, J. Fluid Mech. 322 (1996) 215–241.
[43] C. Geuzaine, J. F. Remacle, Gmsh: a three-dimensional finite element mesh generator with built-in pre- and post-processing facilities, Int. J. Numer. Meth. Eng. 79 (11) (2009) 1309–1331.
[44] C. Cantwell, D. Moxey, A. Comerford, A. Bolis, G. Rocco, G. Mengaldo, D. D. Grazia, S. Yakovlev, J. Lombard, D. Ekelschot, B. Jordi, H. Xu, Y. Mohamied, C. Eskilsson, B. Nelson, P. Vos, C. Biotto, R. Kirby, S. Sherwin, Nektar++: An open-source spectral/hp element framework, Comput. Phys. Commun. 192 (2015) 205–219.
[45] C. Hsiun, C. Chen, Aerodynamic characteristics of a two-dimensional airfoil with ground effect, J. Aircraft 33 (2) (1996) 386–392.
[46] P. Huerre, P. Monkewitz, Local and global instabilities in spatially developing flows, Annu. Rev. Fluid Mech. 22 (1990) 473–537.
[47] L. Li, M. Juniper, Lock-in and quasiperiodicity in a forced hydrodynamically self-excited jet, J. Fluid Mech. 726 (2013) 624–655.
[48] L. Li, M. Juniper, Phase trapping and slipping in a forced hydrodynamically self-excited jet, J. Fluid Mech. 735 (R5) (2013) 1–11.
[49] Y. Zhu, V. Gupta, L. K. Li, Onset of global instability in low-density jets, J. Fluid Mech. 828 (R1).
[50] J. Davitian, D. Getsinger, C. Hendrickson, A. Karagozian, Transition to global instability in transverse-jet shear layers, J. Fluid Mech. 661 (2010) 294–315.
[51] L. Li, M. Juniper, Lock-in and quasiperiodicity in hydrodynamically self-excited flames: Experiments and modelling, P. Combust. Inst. 34 (1) (2013) 947–954.
[52] C. Y. Lee, L. K. Li, M. P. Juniper, R. S. Cant, Nonlinear hydrodynamic and thermoacoustic oscillations of a bluff-body stabilised turbulent premixed flame, Combust. Theor. Model. 20 (1) (2016) 131–153.
[53] G. Rigas, N. P. Jamieson, L. K. Li, M. P. Juniper, Experimental sensitivity analysis and control of thermoacoustic systems, J. Fluid Mech. 787.
[54] S. Balusamy, L. K. Li, Z. Han, M. P. Juniper, S. Hochgreb, Nonlinear dynamics of a self-excited thermoacoustic system subjected to acoustic forcing, P. Combust. Inst. 35 (3) (2015) 3229–3236.
[55] M. Provansal, C. Mathis, L. Boyer, Bénard-von Kármán instability: Transient and forced regimes, J. Fluid Mech. 182 (1987) 1–22.
[56] E. Åkervik, L. Brandt, D. S. Henningson, J. Hœpffner, O. Marxen, P. Schlatter, Steady solutions of the Navier-Stokes equations by selective frequency damping, Phys. Fluids 18 (2006) 068102.
[57] D. Barkely, Linear analysis of the cylinder wake mean flow, Europhys. Lett. 75 (5) (2006) 750–756.
[58] H. Schlichting, Boundary Layer Theory, McGraw-Hill, 7th edn., 1979.